

## Quantifying Time-Averaged Methane Emissions from Individual Coal Mine Vents with GHGSat-D Satellite Observations

Daniel J. Varon,\* Daniel J. Jacob, Dylan Jervis, and Jason McKeever



Cite This: *Environ. Sci. Technol.* 2020, 54, 10246–10253



Read Online

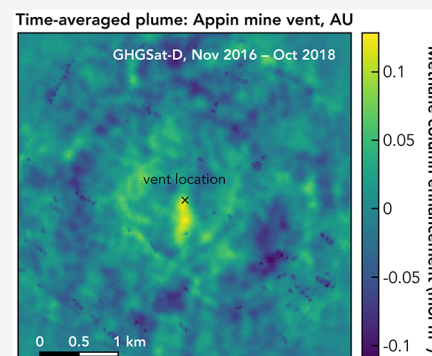
ACCESS |

Metrics & More

Article Recommendations

Supporting Information

**ABSTRACT:** Satellite observations of atmospheric methane plumes offer a means for global mapping of methane point sources. Here we use the GHGSat-D satellite instrument with 50 m effective spatial resolution and 9–18% single-pass column precision to quantify mean source rates for three coal mine vents (San Juan, United States; Appin, Australia; and Bulianta, China) over a two-year period (2016–2018). This involves averaging wind-rotated observations from 14 to 24 overpasses to achieve satisfactory signal-to-noise. Our wind rotation method optimizes the wind direction information for individual plumes to account for error in meteorological databases. We derive source rates from the time-averaged plumes using integrated mass enhancement (IME) and cross-sectional flux (CSF) methods calibrated with large eddy simulations. We find time-averaged source rates ranging from 2320 to 5850 kg h<sup>-1</sup> for the three coal mine vents, with 40–45% precision ( $1\sigma$ ), and generally consistent with previous estimates. The IME and CSF methods agree within 15%. Our results demonstrate the potential of space-based monitoring for annual reporting of methane emissions from point sources and suggest that future satellite instruments with similar pixel resolution but better precision should be able to constrain a wide range of point sources.



### INTRODUCTION

Methane is a powerful greenhouse gas with large anthropogenic sources. It has contributed 1.0 W m<sup>-2</sup> to radiative forcing since preindustrial times on an emission basis.<sup>1</sup> Underground coal mines are estimated to account for ~10% of global anthropogenic methane emissions.<sup>2</sup> Their ventilation shafts are among the largest individual point sources of methane,<sup>3</sup> but individual source estimates are highly uncertain.<sup>4</sup> Remote sensing of atmospheric methane by solar backscatter in the shortwave infrared can be effective for quantifying point sources.<sup>5,6</sup> Krings et al. (2013)<sup>7</sup> used aircraft remote-sensing measurements to quantify methane emissions from coal mine vents in Germany. Frankenberg et al. (2016)<sup>4</sup> observed coal mine plumes in the Four Corners region of the Southwest United States using the airborne AVIRIS-NG spectrometer. Global-observing satellite instruments have demonstrated the capability to characterize methane emissions on regional scales<sup>8–10</sup> and from anomalously large sources<sup>11</sup> but are limited by relatively coarse imaging resolution (~10 km). The GHGSat-D satellite instrument overcomes this limitation by conducting high-resolution observations of point sources over targeted domains.<sup>12</sup> Here we demonstrate the capability of GHGSat-D to observe methane plumes from individual coal mine vents and infer time-averaged source rates.

GHGSat-D was launched in June 2016 as demonstration for a future constellation of small satellites to monitor individual methane point sources from space.<sup>13,14</sup> Single-pass GHGSat-D observations have revealed anomalously high-emitting facilities in oil/gas fields with source rates exceeding 10,000 kg h<sup>-1</sup>.<sup>12</sup>

The largest methane point sources under normal operating conditions are the vents of large underground coal mines, typically in the range of 1000–10,000 kg h<sup>-1</sup>.<sup>4,5,7,15</sup> Here we show that time averaging of wind-rotated GHGSat-D observations can enable detection and quantification of methane emissions from individual coal mine vents, adapting an approach previously applied to satellite observations of point sources for CO,<sup>16</sup> SO<sub>2</sub>,<sup>17,18</sup> NO<sub>2</sub>,<sup>19–21</sup> and NH<sub>3</sub>,<sup>22,23</sup> but including significant innovation to account for large errors and limited number of observations. Time averaging is necessary here to achieve satisfactory signal-to-noise, but it also has the advantage of smoothing over source variability and providing the annual emission estimates most relevant for national emission reporting and global methane budget analyses.

### MATERIALS AND METHODS

**GHGSat-D Observations.** GHGSat-D uses a miniature Fabry–Perot interferometer with a spectral bandpass of 1630–1675 nm.<sup>12,24</sup> The measurements are made at 50 m effective pixel resolution over ~12 × 12 km<sup>2</sup> targeted domains. Methane column concentrations are retrieved from the

Received: February 27, 2020

Revised: July 15, 2020

Accepted: July 16, 2020

Published: July 16, 2020



**Table 1.** Methane Source Rates from Coal Mine Vents Retrieved with GHGSat-D

	San Juan vent	Appin vent	Bulianta vent
	Location		
Country	United States	Australia	China
State/region	New Mexico	New South Wales	Inner Mongolia
Latitude	36.7928°N	34.1815°S	39.3835°N
Longitude	108.3890°W	150.7197°E	110.0951°E
	Source Retrieval Metadata		
Averaging period	Aug 2016–Nov 2018	Nov 2016–Oct 2018	Aug 2016–Dec 2018
Number of clear-sky observations	24	17	14
Single-pass error level	9%	18%	12%
10 m wind speed ( $\text{m s}^{-1}$ ) <sup>a</sup>	3.0 (0.5, 8.0)	2.2 (0.7, 3.8)	3.6 (0.9, 9)
	Source Rate Estimates ( $\text{kg h}^{-1}$ ) <sup>b</sup>		
IME method	$2320 \pm 1050$	$5850 \pm 2360$	$2410 \pm 1000$
CSF method	$2390 \pm 1070$	$4980 \pm 2100$	$2450 \pm 970$
Previous estimates	$360\text{--}2800^c$ , $2585^d$ , $1446^e$	$5200^f$ , $10,800\text{--}12,600^g$	$170^h$

<sup>a</sup>Mean (minimum, maximum) hourly wind speed for the ensemble of GHGSat-D observations, obtained from the GEOS-FP database. <sup>b</sup>Reported source rates are for time-averaged plumes after wind direction optimization (Figure 4) and using either the IME or CSF method. <sup>c</sup>Range from several days of aircraft remote-sensing measurements in April 2015.<sup>4</sup> <sup>d</sup>Annual mean estimate for 2017 from quarterly in situ measurements of flow rate and methane concentration.<sup>40</sup> <sup>e</sup>Mean estimate from five days of in situ aircraft mass-balance measurements.<sup>15</sup> <sup>f</sup>Estimate by Cardno (2009)<sup>41</sup> based on annual coal production activity data and emission factors (converted from  $\text{kt CO}_2 \text{e a}^{-1}$ ). <sup>g</sup>Estimate based on ventilation flow rate and air stream methane concentration from vent design.<sup>29</sup> <sup>h</sup>Estimate from in situ measurements during a weeks-long safety evaluation in 2011.<sup>28</sup>

resulting spectra using a 100-layer, clear-sky radiative transfer model in an inverse modelling framework, following Rodgers (2000)<sup>25</sup> and as described by Varon et al. (2019).<sup>12</sup> The inversion retrieves the total column concentrations  $\Omega(x,y)$  [ $\text{mol m}^{-2}$ ] of methane across the scene, based on HITRAN absorption line spectra<sup>26</sup> and U.S. Standard Atmosphere vertical profiles.<sup>27</sup> The column mass enhancement  $\Delta\Omega(x,y) = \Omega(x,y) - \Omega_b$  then characterizes the plume relative to the local background column concentration  $\Omega_b$  [ $\text{mol m}^{-2}$ ], which is inferred from a scene-wide methane column retrieval.<sup>12</sup> The inversion also retrieves albedo,  $\text{CO}_2$ , and water vapor. The work presented here includes a correction of retrieval errors from aliased surface properties and other measurement parameters.<sup>24</sup>

GHGSat-D has an average revisit time of about two weeks depending on latitude and requires clear skies for successful observation. Since its launch in June 2016, it has repeatedly targeted the vents of three underground coal mines: the San Juan mine in New Mexico, USA; the Appin mine in New South Wales, Australia; and the Bulianta mine in Inner Mongolia, China. These coal mines were selected for their large coal production rates and/or previous reports of large methane emissions.<sup>4,15,28,29</sup> Here, we examine GHGSat-D observations of the coal mine vents taken between August 2016 and December 2018, totaling 14–24 cloud-free observations per mine (see Table 1). The Appin mine was closed on 28 June 2017 because of safety concerns and partially reopened on 13 October 2017. The four cloud-free observations made during this extended closure may reflect lower emissions than under normal operating conditions. Several other shorter closures occurred at Appin during the observation period, but these did not overlap with our measurements.

Figure 1 shows methane column enhancements from individual GHGSat-D scenes centered on the San Juan coal mine vent. The geolocation of the retrieved column enhancements is accurate to within ~30 m.<sup>24</sup> These scenes were chosen for their detectable plumes but also illustrate GHGSat-D retrieval artefacts resulting primarily from striping noise,

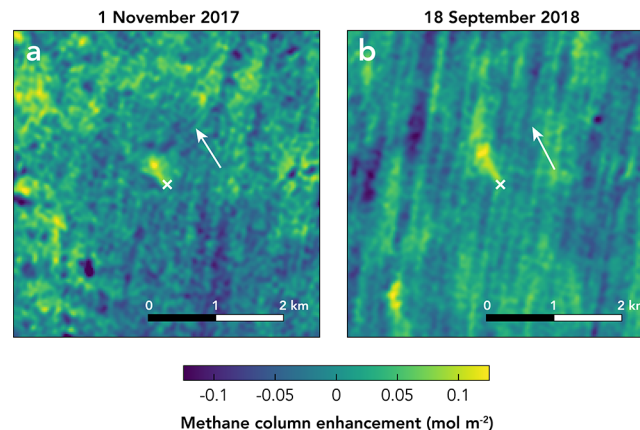


**Figure 1.** Instantaneous plumes observed by GHGSat-D over the San Juan mine in New Mexico on (a) November 1st, 2017, and (b) September 18th, 2018. The white “x” symbols mark the location of the coal mine vent ( $36.7928^\circ\text{N}$ ,  $108.3890^\circ\text{W}$ ) and the white arrows show the instantaneous local wind direction inferred from the orientation of the plumes (see the “Wind Data for Time Averaging” section).

surface reflectance variability, and stray light. Some artefacts are similar in magnitude to the plumes, which highlights the importance of prior knowledge of source location. Column precisions for our San Juan, Appin, and Bulianta observations are estimated at 9, 18, and 12% of background, respectively, based on the standard deviations of nonplume column enhancements across the scenes. Most scenes do not feature readily detectable plumes, which motivates our time-averaging analysis.

**Wind Data for Time-Averaging.** Time averaging of plume observations to improve signal-to-noise and infer emissions from point sources requires knowledge of wind speed and direction for the individual scenes.<sup>16–23,30</sup> Wind information can come from local measurements, from assimilated meteorological databases, or directly from the plume observations themselves.<sup>31</sup> The appropriate wind-averaging time for an individual scene depends on the lifetime

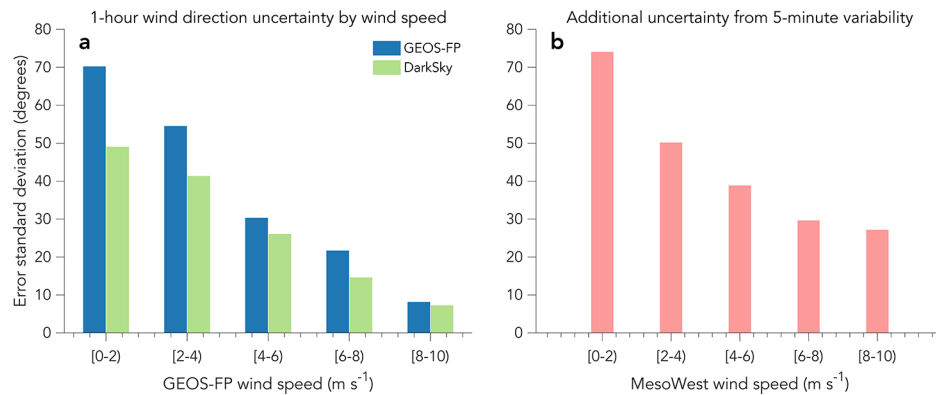


**Figure 2.** Error in estimating 10 m wind direction from the GEOS-FP and DarkSky datasets. (a) Error standard deviations for GEOS-FP and DarkSky hourly average wind direction relative to one month of measurements from 10 U.S. airports (ABQ, ATL, BOS, DFW, LAX, MCI, MSP, PDX, PHL, and PHX) in the MesoWest database, binned by GEOS-FP wind speed. The airport measurements are for daytime June 2017 (15:00–21:00 UTC). (b) Additional uncertainty for estimating 5 min wind direction from 1 h averages, based on 5 min wind direction variability in the MesoWest data.

of the detectable plume before turbulent diffusion dilutes it to below detectable levels. It ranges from ~5 min for a typical plume (<1 km) to ~1 h for a very large plume several km in extent.<sup>32</sup> Short averaging times produce higher source rate retrieval errors because of added uncertainty from subhourly wind variability. Coal mine vent plumes as observed by GHGSat-D tend to be <1 km in scale (Figure 1) and are therefore best interpreted with a short averaging time of about 5 min.

Our algorithm to relate plume concentrations to emissions uses 10 m wind information.<sup>32</sup> We take this information from two hourly meteorological databases: (1) the NASA Goddard Earth Observing System—Fast Processing (GEOS-FP) reanalysis product with full global coverage at  $0.25^\circ \times 0.3125^\circ$  resolution<sup>33</sup> and (2) the DarkSky online weather application programming interface with partial coverage.<sup>34</sup> Comparison with one month of daytime (15:00–21:00 UTC) wind measurements from 10 U.S. airports in the MesoWest database<sup>35</sup> suggests that GEOS-FP has more precise wind speed data than DarkSky, while DarkSky has more precise wind direction data. Error standard deviations on hourly average wind speed and direction from GEOS-FP are  $1.5 \text{ m s}^{-1}$  and  $49^\circ$  relative to the airport measurements, compared to  $2.2 \text{ m s}^{-1}$  and  $37^\circ$  for DarkSky. We therefore use GEOS-FP wind speed and direction as default, but substitute DarkSky wind direction where available. DarkSky winds are available for nearly all our observations of the San Juan and Appin mines, but not for Bulianta.

Figure 2 shows the wind direction error statistics when using meteorological reanalysis data to infer local wind direction as referenced by the MesoWest database. The error depends strongly on wind speed, with larger errors for low wind speeds, as would be expected from turbulence. Uncertainty in the mean hourly wind in the meteorological databases (Figure 2a) is calculated as the standard deviation of the residuals between hourly GEOS-FP (or DarkSky) and MesoWest wind directions. Wind direction errors for both GEOS-FP and DarkSky are binned by GEOS-FP wind speed, which is the wind speed we use to estimate source rates (see the “Estimating Source Rates” section). This error is compounded for small plumes by the error in inferring the more appropriate 5 min average wind (Figure 2b), in which case the two errors are added in quadrature. We calculate this additional error as

the standard deviation of the residuals between the hourly and 5 min MesoWest wind directions. For observations with strong instantaneous plumes detectable by eye (Figure 1), we estimate wind direction directly from the plume axis, which we define from a weighted mean of pixel coordinates with the plume column concentrations as weights. The wind direction error in that case is set to  $5^\circ$  to account for error in the retrieved methane columns.

For a given point source, a time-averaged plume over the GHGSat-D record can be constructed from the methane column enhancements  $\Delta\Omega_i(x,y)$  [ $\text{mol m}^{-2}$ ] observed over the source domain ( $x, y$ ) on individual days  $i = 1\dots N$ . This is done by (1) georeferencing the observations and aligning them by linear interpolation to the grid of the first observation, (2) rotating each observation around the known source location by the local wind direction  $\theta_i$ , and (3) computing perpixel means over the rotated observations remapped to the common grid. The alignment and rotation steps require precise knowledge of the source location at the scale of the observations. The rotation step may introduce negative bias from wind direction uncertainty, as a misrotated plume may be lost in the noisy background of the time-averaged observation. We account for this bias through our source rate retrieval method, as described in the “Estimating Source Rates” section below.

**Optimizing Wind Directions.** Wind direction errors in the meteorological databases are relatively large, particularly under low wind conditions (Figure 2). Here, we correct the wind directions used for plume rotation in order to maximize concentrations in the time-averaged plume while minimizing deviation from prior wind estimates. Specifically, we maximize the joint Gaussian probability distribution  $P(\boldsymbol{\theta})$  given by

$$\log P(\boldsymbol{\theta}) = -\frac{(M(\boldsymbol{\theta}) - M_{\max})^2}{\delta^2} - (\boldsymbol{\theta} - \boldsymbol{\theta}_a)^T S_a^{-1} (\boldsymbol{\theta} - \boldsymbol{\theta}_a) \quad (1)$$

by minimizing  $-\log P(\boldsymbol{\theta})$ . Here,  $\boldsymbol{\theta}$  is a wind direction vector whose elements  $\theta_i, i = 1\dots N$ , are the wind directions used to rotate  $N$  GHGSat-D observations;  $\boldsymbol{\theta}_a$  is a vector of prior wind direction estimates for the observations, from GEOS-FP and DarkSky;  $S_a$  is the (diagonal) prior error covariance matrix describing uncertainty in the prior wind direction, which depends on wind speed, plume lifetime (here, 5 min), and whether the prior is drawn from GEOS-FP, DarkSky, or the

plume itself;  $M(\theta)$  [mol] is the total methane mass [integrated mass enhancement (IME)] in a wedge-shaped mask placed downwind of the source after time-averaging with a set of wind directions  $\theta$  (see below);  $M_{\max}$  [mol] is the maximum possible value of  $M(\theta)$  for the set of observations when no constraints are placed on  $\theta$ ; and  $\delta^2$  [mol<sup>2</sup>] is the error variance in  $M(\theta)$  due to GHGSat-D measurement noise. We minimize  $-\log P(\theta)$  numerically using the Nelder–Mead simplex algorithm.<sup>36,37</sup>

We rotate individual observations by their wind direction such that the time-averaged rotated wind is by convention from the north.  $M(\theta)$  is computed at each iteration of the optimization procedure as the IME over a simple wedge-shaped mask extending 500 m south and  $\pm 15^\circ$  of south. The IME is the sum of column enhancements  $\overline{\Delta\Omega}(x,y)$  over the mask, multiplied by the pixel area. We then compute  $M_{\max}$  by rotating the mask around the source location by  $360^\circ$  in each observation, recording for each the maximum IME, and averaging over all observations. To calculate  $\delta$ , we perform time averaging using our prior wind directions and then compute the IME within the wedge-shaped mask when placed at 100 random nonplume locations across the time-averaged domain; the standard deviation of these results gives  $\delta$ .

Optimizing wind directions to enhance plume mass introduces a risk of aliasing positive measurement artefacts into the time-averaged plume. This problem is mitigated by the prior wind direction term in eq 1, which penalizes the optimizer for straying too far from reanalysis wind direction estimates. To assess the remaining risk, we conduct a series of null tests, optimizing winds for our observations of the San Juan mine with the wind-rotated average centered on four false source locations (Figure S1). The results indicate a minor effect and are described in the Supporting Information.

**Defining Plume Boundaries.** Inferring source rates from plume observations requires a mask that distinguishes plume pixels from the background. Varon et al. (2018)<sup>32</sup> suggested a *t*-test procedure for isolating plumes from normally distributed measurement noise, but that procedure's performance is limited here by systematic errors in the time-averaged observations. Instead, we isolate the plumes by applying an enhancement threshold at the 98th percentile of  $\overline{\Delta\Omega}(x,y)$  over the time-averaged domain. This defines a binary threshold mask for the scene. To delete random classification errors and reduce loss of plume enhancements at mask edges because of thresholding, we smooth the masks with a  $150 \times 150$  m<sup>2</sup> median filter, which replaces each pixel's value with the median of its  $150 \times 150$  m<sup>2</sup> neighborhood, followed by a Gaussian filter with a standard deviation of 50 m. A final threshold is applied to produce a smooth, binary plume mask. Wind rotation and time averaging smooth out most of the observation artefacts such as those seen in Figure 1, but some still appear in the mask. For the purpose of inferring point source rates, we only consider the continuous portion of the mask originating from the source location.

The plume-masking scheme can strongly influence source rate retrieval results because it determines which measurement pixels are included in the analysis and which are not. The retrieval must therefore be calibrated according to the chosen scheme. We discuss this process in the next section.

**Estimating Source Rates.** We estimate source rates for our time-averaged plumes using two different methods: the IME method and the cross-sectional flux (CSF) method.<sup>32</sup> The IME method relates the source rate  $Q$  [mol s<sup>-1</sup>] to the

detectable plume mass IME [mol] in terms of an effective wind speed  $U_{\text{eff,IME}}$  [m s<sup>-1</sup>] and plume size  $L$  [m]:

$$Q = \frac{U_{\text{eff,IME}}}{L} \text{IME} = \frac{U_{\text{eff,IME}}}{L} \sum_{j=1}^n \overline{\Delta\Omega}(x_j, y_j) A_j \quad (2)$$

where  $\overline{\Delta\Omega}(x_j, y_j)$ ,  $j = 1 \dots n$ , is the time-averaged column concentration of the  $j$ th plume pixel with coordinates  $(x_j, y_j)$  and area  $A_j$  and the summation is over the  $n$  pixels within the continuous plume mask originating from the source location. The plume size  $L$  is defined following Varon et al. (2018)<sup>32</sup> as the square root of the plume mask's area. The effective wind speed  $U_{\text{eff,IME}}$  is an operational parameter that is inferred from the local 10 m wind speed  $U_{10}$  in a manner that depends on the definitions of the plume mask and size. We discuss the  $U_{\text{eff}} = f(U_{10})$  relationship below.

The CSF method originally introduced by White (1976)<sup>38</sup> and adapted to column observations by Krings et al. (2011, 2013)<sup>7,39</sup> and Varon et al. (2018)<sup>32</sup> relates  $Q$  to a cross-plume concentration integral [mol m<sup>-1</sup>] and a different effective wind speed  $U_{\text{eff,CSF}}$  than in the IME method:

$$Q = U_{\text{eff,CSF}} \int_a^b \overline{\Delta\Omega}(x, y) dy \quad (3)$$

Here, the  $x$ -axis is defined by the wind direction (northerly by convention for our time-averaged plumes) and the  $y$ -axis is perpendicular to the wind direction. The integral is computed between the plume boundaries [ $a, b$ ] defined by the plume mask, and this computation can be done at multiple downwind distances  $x$  to improve estimation of  $Q$  through averaging. Here, we repeat the calculation at pixel-width intervals across the full extent of the detectable plume. The effective wind speeds in the IME and CSF methods are operational parameters that can be related to the local 10 m wind speed  $U_{10}$ . Varon et al. (2018)<sup>32</sup> calibrated  $U_{\text{eff}} = f(U_{10})$  relationships for instantaneous plumes generated by large eddy simulation (LES), but the relationships may be different here for two reasons. First, we use a different definition of the plume mask, as described in the previous section. This affects the dependence of IME and plume transects on  $Q$ . Second, the dependences of IME (or plume transects) on wind speed and source rate may be different for time-averaged compared to instantaneous plumes.

Here, we calibrate new  $U_{\text{eff}} = f(U_{10})$  relationships for the IME and CSF methods, customized to our observing conditions and plume mask. To do this, we repeat the LES plume analysis of Varon et al. (2018)<sup>32</sup> on the same ensemble of simulations, but with time-averaged rather than instantaneous plumes. The LES ensemble comprises fifteen 5 h simulations with a range of wind speeds and boundary layer depths. We calibrate  $U_{\text{eff}} = f(U_{10})$  relationships for each coal mine independently because for each we have a different number of observations and level of background noise. We use the following procedure. First, a number of LES plume snapshots are randomly drawn from the ensemble (24 for San Juan, 17 for Appin, and 14 for Bulianta). The source rate for the plumes is set to a random (constant) value between 1000 and 6000 kg h<sup>-1</sup>, typical for large coal mine vent emissions.<sup>5</sup> Each snapshot is rotated by a random wind direction, and the 5 min average value of  $U_{10}$  at the source location is recorded. We corrupt the plume snapshots with normally distributed, spatially uncorrelated noise of mean zero and standard

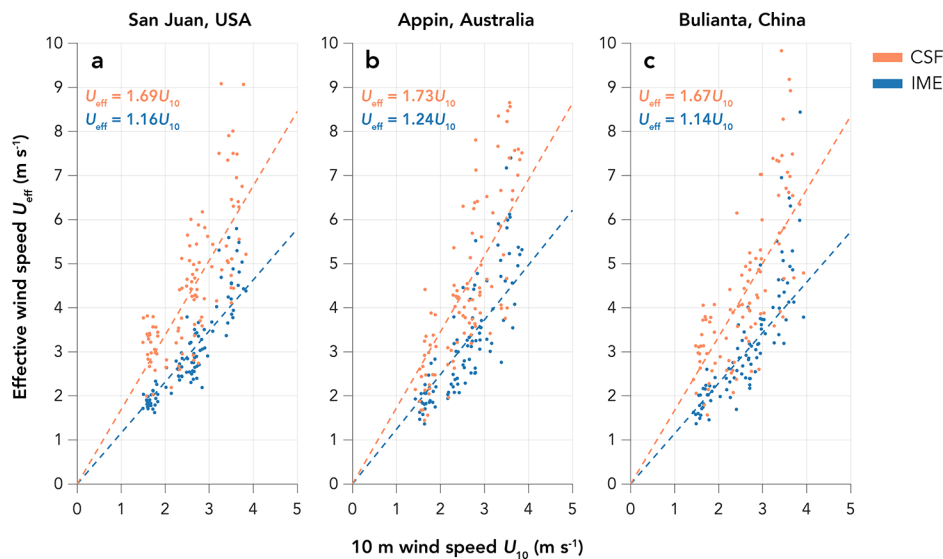


**Figure 3.** Effective wind speeds  $U_{\text{eff}}$  for retrieving time-averaged methane source rates by the IME and CSF methods (eqs 2 and 3) as a function of the time-averaged 10 m wind speed  $U_{10}$ . The  $U_{\text{eff}} = f(U_{10})$  relationships are derived from LESs of instantaneous methane plumes, with time averaging and wind rotation corresponding to our measurement conditions for (a) San Juan, (b) Appin, and (c) Bulianta. Each point represents a time-averaged plume assembled from LES instantaneous plumes, with the level of background noise and number of observations adapted to the mine of interest (see Table 1). The functions are fit by robust least squares (see text).

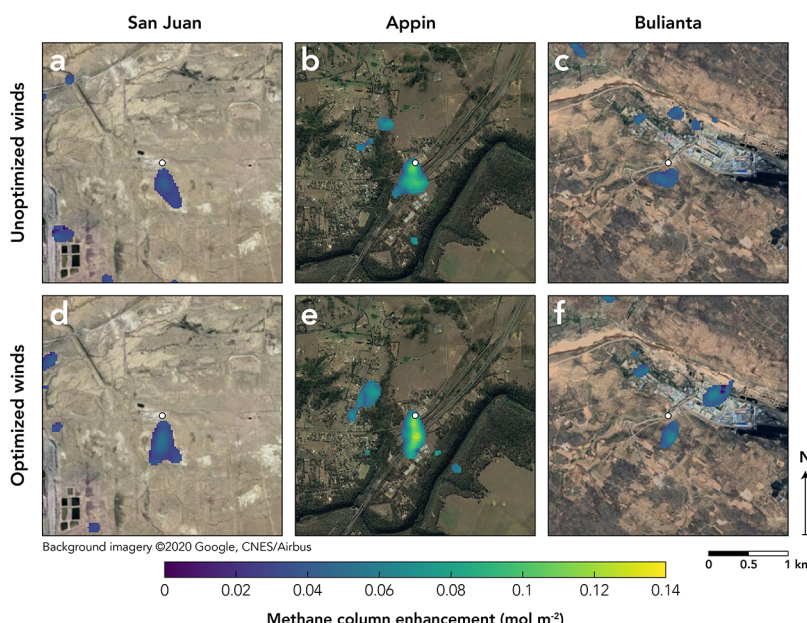


**Figure 4.** Time-averaged methane plumes from the San Juan, Appin, and Bulianta coal mine vents, as observed by GHGSat-D from August 2016 through December 2018. The single-pass observations have been rotated to a northerly wind direction using (a–c) local wind data from GEOS-FP and DarkSky and (d–f) optimized wind directions with GEOS-FP and DarkSky winds as prior estimates (see the “Optimizing Wind Directions” section). The methane column enhancements are overlaid on Google Earth Pro imagery after thresholding and smoothing the plume masks with median and Gaussian filters (see the “Defining Plume Boundaries” section). The white markers show the location of the coal mine vent in the center of each scene.

deviation dependent on the observation conditions of each mine (9, 18, or 12% of a 1850 ppb background). We then follow the wind direction optimization procedure outlined above (eq 1) to recover the LES plume wind directions from the randomly corrupted prior estimates, and assemble in this manner a time-averaged plume pseudo-observation. After constructing the plume mask and calculating IME,  $L$ , and the mean transect for the time-averaged plume, we use eqs 2 and 3 to compute  $U_{\text{eff}}$  based on prior knowledge of  $Q$ . Meanwhile, we compute  $U_{10}$  for the time-averaged observation

as the mean of the 5 min averages across aggregated plumes. We repeat this procedure 100 times on a set of LES plumes comprising 80% of the ensemble (~2900 plume snapshots), simulating 100 time-averaged plumes with different mean source rates. We then derive the  $U_{\text{eff}} = f(U_{10})$  relationships by least squares fitting. Finally, to quantify source rate retrieval error, we evaluate these relationships on time-averaged plumes constructed from the remaining 20% of the LES plume ensemble (see the Supporting Information).

Figure 3 shows our derived  $U_{\text{eff}} = f(U_{10})$  relationships for the three coal mines. We find that linear relationships without intercepts capture the behavior well in all cases, and that the slopes are similar despite differences in the number of observations aggregated, level of measurement noise, and wind direction prior error variance. The winds are fit by robust linear regression, which assigns less weight to outlier points, to mitigate the considerable scatter in  $U_{\text{eff}}$  for larger values of  $U_{10}$ . Plume enhancements in these outlier cases are very low and difficult to detect, even after wind direction optimization.  $U_{\text{eff}} = f(U_{10})$  slopes for the CSF method are similar to the results of Varon et al. (2018),<sup>32</sup> but slopes for the IME method are significantly different, which would reflect different interdependences between plume shape, mass, and ventilation time for time-averaged plumes compared to instantaneous plumes.

## RESULTS AND DISCUSSION

**Time-Averaged Plumes.** Figure 4 shows our time-averaged rotated observations of the San Juan, Appin, and Bulianta coal mine vents, both before and after wind direction optimization. The plumes are oriented to the south of the source location by convention and are separated from the noisy background by thresholding and smoothing as discussed in the “Defining Plume Boundaries” section. Enhancements above the threshold but not directly downwind of the source location are ignored as retrieval artefacts. We can make this distinction because wind-rotated time averaging with variable wind direction destroys spatial continuity between observations. Time-averaged enhancements lying outside of the downwind area should be classified as artefacts unless they are identified as plausible plumes in single-pass observations, particularly under low-wind conditions in which plumes may have highly complex shapes, which is not the case here.

Before optimizing wind direction to improve plume-to-noise contrast, the San Juan and Appin mine vents show strong time-averaged plumes with respective peak enhancements 7 and 17% above background. The Bulianta mine vent shows peak downwind enhancements 8% above background, but a less distinctive plume shape. One possible explanation for this is that the Bulianta vent is at the base of a hill, leading to large and potentially systematic wind direction error, in contrast to the San Juan and Appin vents, which are in flat terrain. Optimizing wind direction amplifies the plumes’ mean enhancements by 11–13% and produces a more elongated plume shape for the Bulianta coal mine, with peak methane enhancements more than 10% above background. Peak plume enhancements do not generally appear at the source location, contrary to what one would expect. This could be because of systematic retrieval errors over the vent location (e.g. because of surface reflectance variability or aerosol particles in the plume). Source pixel enhancements may also be lower than downwind pixel enhancements because the plume is present in only part of the source pixel along the wind direction. We expect this effect to be weaker at fine spatial scales than previously documented for the TROPOMI satellite instrument’s kilometer-scale pixels.<sup>11</sup> Finally, intrapixel variations in methane concentration can produce errors from nonlinearity in the column retrieval algorithm. Missing large enhancements near the vent could lead to a low bias in IME emission rate estimates, but would have a smaller effect on the CSF method, where each cross-plume integral downwind of the source independently approximates the emissions.

**Time-Averaged Source Rates.** Table 1 shows our time-averaged source rate estimates for the San Juan, Appin, and Bulianta mines determined from the wind-optimized plumes. Estimates from the IME and CSF methods agree within their error standard deviations, which is a first check that our effective wind speed functions are well-calibrated. We estimate mean emissions of  $2320 \pm 1050 \text{ kg h}^{-1}$  for the San Juan vent,  $5850 \pm 2360 \text{ kg h}^{-1}$  for the Appin vent, and  $2410 \pm 1000 \text{ kg h}^{-1}$  for the Bulianta vent using the IME method. Using the CSF method, the estimates are 2–3% higher for San Juan and Bulianta, but 15% lower for Appin, contradicting the prospect of low bias in the IME method. The reported uncertainties ( $1\sigma$ ) are 40–45% and incorporate wind speed error, error in the IME and CSF models (including wind direction error and uncertainty in the effective wind speed fits of Figure 3), correlated random measurement noise in the retrieved columns, and error from source variability. We assess wind speed error by comparing GEOS-FP and MesoWest wind data, model error by evaluating source rate retrievals on a test set of synthetic time-averaged plumes, and measurement error by randomly sampling GHGSat-D background noise. We estimate the error from source variability using daily ground-based emission estimates for three coal mine ventilation shafts in China from 2007 to 2009, provided to us by Raven Ridge Resources, Inc. (Figure S2). We add these errors in quadrature to obtain our final error estimates. A detailed error analysis is presented in the Supporting Information.

Also shown in Table 1 are previous emission estimates for each of the coal mine vents, all from much smaller samples and/or durations. Frankenberg et al. (2016)<sup>4</sup> estimated emissions of  $360\text{--}2800 \text{ kg h}^{-1}$  for the San Juan vent based on several days of aircraft remote-sensing measurements, and Smith et al. (2017)<sup>15</sup> inferred mean emissions of  $1446 \text{ kg h}^{-1}$  from five days of aircraft mass-balance measurements during the same period. Quarterly in situ measurements of the vent flow rate and methane concentration reported to the United States Environmental Protection Agency (EPA) in 2017 put emissions from the San Juan vent at  $2585 \text{ kg h}^{-1}$  averaged over the year,<sup>40</sup> in remarkable agreement with our estimate. Ong et al. (2017)<sup>29</sup> approximated emissions of  $10,800\text{--}12,600 \text{ kg h}^{-1}$  from the Appin mine, based on estimates of the vent flow rate and air stream methane concentration. Cardno (2009)<sup>41</sup> used coal production activity data and Australian National Greenhouse Accounts (NGA) emission factors to estimate ventilation shaft methane emissions of  $\sim 5200 \text{ kg h}^{-1}$  for the Appin mine in a two longwall mining formation. We are aware of only one emission estimate for the Bulianta mine:  $170 \text{ kg h}^{-1}$ , reported by the Chinese State Administration for Coal Mine Safety (SACMS).<sup>28</sup> This estimate is based on ground measurements made during a 2–3 month safety evaluation performed in 2011 and is much lower than our result.

In summary, our results demonstrate the capability of space-based observations of methane plumes to quantify point source rates from high-emitting facilities under apparently normal operating conditions. The GHGSat-D demonstration satellite instrument used in our work has fine spatial resolution (50 m) but coarse single-pass column retrieval precision (9–18%) and large retrieval artefacts. Nevertheless, we were able to quantify time-averaged methane emissions from large coal mine vents ( $>1000 \text{ kg h}^{-1}$ ) with ~40% uncertainty. This involved averaging 14–24 observations per target over a 2 year period, using an optimized wind rotation procedure. Our time-averaged result for the San Juan coal mine vent was in close

agreement with the annual emission reported to the U.S. EPA. Future methane-observing satellite instruments with similar spatial resolution but improved precision, including GHGSat-C1 to launch in 2020<sup>42</sup> and the next generation of orbiting hyperspectral surface imagers,<sup>43</sup> will likely improve our ability to detect methane plumes from individual facilities and infer source rates. Quantifying sources down to 100 kg h<sup>-1</sup> would account for more than 90% of emissions from point sources in the U.S. GHGRP.<sup>5</sup> Such thresholds for detection and quantification will continue to shrink as revisit rates for time averaging increase with the number of instruments in orbit.<sup>30</sup> Repeated measurements from satellites may be particularly useful for estimating annual emissions for facility-level reporting purposes.

## ASSOCIATED CONTENT

### Supporting Information

The Supporting Information is available free of charge at <https://pubs.acs.org/doi/10.1021/acs.est.0c01213>.

Wind direction optimization null tests and source rate retrieval error analysis ([PDF](#))

## AUTHOR INFORMATION

### Corresponding Author

Daniel J. Varon — Harvard University, Cambridge, Massachusetts 02138, United States; GHGSat Inc., Montréal, Québec H2W 1Y5, Canada;  [orcid.org/0000-0002-3207-5731](http://orcid.org/0000-0002-3207-5731); Email: [danielvaron@g.harvard.edu](mailto:danielvaron@g.harvard.edu)

### Authors

Daniel J. Jacob — Harvard University, Cambridge, Massachusetts 02138, United States  
Dylan Jervis — GHGSat Inc., Montréal, Québec H2W 1Y5, Canada  
Jason McKeever — GHGSat Inc., Montréal, Québec H2W 1Y5, Canada

Complete contact information is available at:

<https://pubs.acs.org/10.1021/acs.est.0c01213>

### Notes

The authors declare no competing financial interest.

## ACKNOWLEDGMENTS

We thank O. B. A. Durak and J. J. Sloan for their roles in developing the GHGSat retrieval algorithm and measurement concept. We thank C. Herzog, M. Arias, K. Wisniewski, M. Latulippe, N. Brown, and J. Thompson for technical assistance and preparation of the GHGSat-D methane data. We also thank J. D. Maasakkers for helpful discussion. This research was funded by GHGSat, Inc. D.J.J. acknowledges support from the Carbon Monitoring System of the NASA Earth Science Division.

## REFERENCES

- (1) International Panel on Climate Change (IPCC). *Climate Change 2013: The Physical Science Basis. Contribution Of Working Group I to the Fifth Assessment Report Of the Intergovernmental Panel On Climate Change*; IPCC, Cambridge University Press: New York, 2013.
- (2) Saunois, M.; Bousquet, P.; Poulter, B.; Peregon, A.; Ciais, P.; Canadell, J. G.; Dlugokencky, E. J.; Etiope, G.; Bastviken, D.; Houweling, S.; Janssens-Maenhout, G.; Tubiello, F. N.; Castaldi, S.; Jackson, R. B.; Alexe, M.; Arora, V. K.; Beerling, D. J.; Bergamaschi, P.; Blake, D. R.; Brailsford, G.; Brovkin, V.; Bruhwiler, L.; Crevoisier, C.; Crill, P.; Covey, K.; Curry, C.; Frankenberger, C.; Gedney, N.; Höglund-Isaksson, L.; Ishizawa, M.; Ito, A.; Joos, F.; Kim, H.-S.; Kleinen, T.; Krummel, P.; Lamarque, J.-F.; Langenfelds, R.; Locatelli, R.; Machida, T.; Maksyutov, S.; McDonald, K. C.; Marshall, J.; Melton, J. R.; Morino, I.; Naik, V.; Patra, S.; Parmentier, F.-J. W.; Patra, P. K.; Peng, C.; Peng, S.; Peters, G. P.; Pison, I.; Prigent, C.; Prinn, R.; Ramonet, M.; Riley, W. J.; Saito, M.; Santini, M.; Schroeder, R.; Simpson, I. J.; Spahni, R.; Steele, P.; Takizawa, A.; Thornton, B. F.; Tian, H.; Tohjima, Y.; Viovy, N.; Voulgarakis, A.; van Weele, M.; van der Werf, G. R.; Weiss, R.; Wiedinmyer, C.; Wilton, D. J.; Wiltshire, A.; Worthy, D.; Wunch, D.; Xu, X.; Yoshida, Y.; Zhang, B.; Zhang, Z.; Zhu, Q. The Global Methane Budget 2000–2012. *Earth Syst. Sci. Data* **2016**, *8*, 697–751.
- (3) Maasakkers, J. D.; Jacob, D. J.; Sulprizio, M. P.; Turner, A. J.; Weitz, M.; Wirth, T.; Hight, C.; DeFigueiredo, M.; Desai, M.; Schmeltz, R.; Hockstad, L.; Bloom, A. A.; Bowman, K. W.; Jeong, S.; Fischer, M. L. Gridded National Inventory of U.S. Methane Emissions. *Environ. Sci. Technol.* **2016**, *50*, 13123–13133.
- (4) Frankenberger, C.; Thorpe, A. K.; Thompson, D. R.; Hulley, G.; Kort, E. A.; Vance, N.; Borchardt, J.; Krings, T.; Gerilowski, K.; Sweeney, C.; Conley, S.; Bue, B. D.; Aubrey, A. D.; Hook, S.; Green, R. O. Airborne methane remote measurements reveal heavy-tail flux distribution in Four Corners region. *Proc. Natl. Acad. Sci. U.S.A.* **2016**, *113*, 9734–9739.
- (5) Jacob, D. J.; Turner, A. J.; Maasakkers, J. D.; Sheng, J.; Sun, K.; Liu, X.; Chance, K.; Aben, I.; McKeever, J.; Frankenberger, C. Satellite observations of atmospheric methane and their value for quantifying methane emissions. *Atmos. Chem. Phys.* **2016**, *16*, 14371–14396.
- (6) Duren, R. M.; Thorpe, A. K.; Foster, K. T.; Rafiq, T.; Hopkins, F. M.; Yadav, V.; Bue, B. D.; Thompson, D. R.; Conley, S.; Colombi, N. K.; Frankenberger, C.; McCubbin, I. B.; Eastwood, M. L.; Falk, M.; Herner, J. D.; Croes, B. E.; Green, R. O.; Miller, C. E. California's methane super-emitters. *Nature* **2019**, *575*, 180–184.
- (7) Krings, T.; Gerilowski, K.; Buchwitz, M.; Hartmann, J.; Sachs, T.; Erzinger, J.; Burrows, J. P.; Bovensmann, H. Quantification of methane emission rates from coal mine ventilation shafts using airborne remote sensing data. *Atmos. Meas. Tech.* **2013**, *6*, 151–166.
- (8) Turner, A. J.; Jacob, D. J.; Wecht, K. J.; Maasakkers, J. D.; Lundgren, E.; Andrews, A. E.; Biraud, S. C.; Boesch, H.; Bowman, K. W.; Deutscher, N. M.; Dubey, M. K.; Griffith, D. W. T.; Hase, F.; Kuze, A.; Notholt, J.; Ohyama, H.; Parker, R.; Payne, V. H.; Sussmann, R.; Sweeney, C.; Velazco, V. A.; Warneke, T.; Wennberg, P. O.; Wunch, D. Estimating global and North American methane emissions with high spatial resolution using GOSAT satellite data. *Atmos. Chem. Phys.* **2015**, *15*, 7049–7069.
- (9) Maasakkers, J. D.; Jacob, D. J.; Sulprizio, M. P.; Scarpelli, T. R.; Nesser, H.; Sheng, J.-X.; Zhang, Y.; Hersher, M.; Bloom, A. A.; Bowman, K. W.; Worden, J. R.; Janssens-Maenhout, G.; Parker, R. J. Global distribution of methane emissions, emission trends, and OH concentrations and trends inferred from an inversion of GOSAT satellite data for 2010–2015. *Atmos. Chem. Phys.* **2019**, *19*, 7859–7881.
- (10) Miller, S. M.; Michalak, A. M.; Detmers, R. G.; Hasekamp, O. P.; Bruhwiler, L. M. P.; Schwietzke, S. China's coal mine methane regulations have not curbed growing Emissions. *Nat. Commun.* **2019**, *10*, 303.
- (11) Pandey, S.; Gautam, R.; Houweling, S.; van der Gon, H. D.; Sadavarte, P.; Borsdorff, T.; Hasekamp, O.; Landgraf, J.; Tol, P.; van Kempen, T.; Hoogeveen, R.; van Hees, R.; Hamburg, S. P.; Maasakkers, J. D.; Aben, I. Satellite observations reveal extreme methane leakage from a natural gas well blowout. *Proc. Natl. Acad. Sci. U.S.A.* **2019**, *116*, 26376–26381.
- (12) Varon, D. J.; McKeever, J.; Jervis, D.; Maasakkers, J. D.; Pandey, S.; Houweling, S.; Aben, I.; Scarpelli, T.; Jacob, D. J. Satellite discovery of anomalously large methane emissions from oil/gas production. *Geophys. Res. Lett.* **2019**, *46*, 13507–13516.
- (13) Brakeboer, B. N. A. Development of the structural and thermal control subsystems for an Earth observation microsatellite and its payload. M.Sc. Thesis, University of Toronto, 2015.

- (14) Sloan, J. J.; Durak, B.; Gains, D.; Ricci, F.; McKeever, J.; Lamorie, J.; Sdao, M.; Latendresse, V.; Lavoie, J.; Kruzelecky, R. Fabry-Perot interferometer based satellite detection of atmospheric trace gases. U.S. Patent 9,228,897 B2, 2016, United States Patent and Trademark Office. Retrieved from <https://patentimages.storage.googleapis.com/85/4e/65/b3f964823f2f3b/US9228897.pdf>.
- (15) Smith, M. L.; Gvakharia, A.; Kort, E. A.; Sweeney, C.; Conley, S. A.; Faloona, I.; Newberger, T.; Schnell, R.; Schwietzke, S.; Wolter, S. Airborne Quantification of Methane Emissions over the Four Corners Region. *Environ. Sci. Technol.* **2017**, *51*, 5832–5837.
- (16) Pommier, M.; McLinden, C. A.; Deeter, M. Relative changes in CO emissions over megacities based on observations from space. *Geophys. Res. Lett.* **2013**, *40*, 3766–3771.
- (17) Fioletov, V. E.; McLinden, C. A.; Krotkov, N.; Li, C. Lifetimes and emissions of SO<sub>2</sub> from point sources estimated from OMI. *Geophys. Res. Lett.* **2015**, *42*, 1969–1976.
- (18) McLinden, C. A.; Fioletov, V.; Shephard, M. W.; Krotkov, N.; Li, C.; Martin, R. V.; Moran, M. D.; Joiner, J. Space-based detection of missing sulfur dioxide sources of global air pollution. *Nat. Geosci.* **2016**, *9*, 496–500.
- (19) Valin, L. C.; Russell, A. R.; Cohen, R. C. Variations of OH radical in an urban plume inferred from NO<sub>2</sub> column measurements. *Geophys. Res. Lett.* **2013**, *40*, 1856–1860.
- (20) De Foy, B.; Lu, Z.; Streets, D. G.; Lamsal, L. N.; Duncan, B. N. Estimates of power plant NO<sub>x</sub> emissions and lifetimes from OMI NO<sub>2</sub> satellite retrievals. *Atmos. Environ.* **2015**, *116*, 1–11.
- (21) Zhang, Y.; Gautam, R.; Zavala-Araiza, D.; Jacob, D. J.; Zhang, R.; Zhu, L.; Sheng, J. X.; Scarpelli, T. Satellite observed changes in Mexico's offshore gas flaring activity linked to oil/gas regulations. *Geophys. Res. Lett.* **2019**, *46*, 1879–1888.
- (22) Clarisse, L.; Van Damme, M.; Clerbaux, C.; Coheur, P.-F. Tracking down global NH<sub>3</sub> point sources with wind-adjusted superresolution. *Atmos. Meas. Tech.* **2019**, *12*, 5457–5473.
- (23) Dammers, E.; McLinden, C. A.; Griffin, D.; Shephard, M. W.; Van Der Graaf, S.; Lutsch, E.; Schaap, M.; Gainairu-Matz, Y.; Fioletov, V.; Van Damme, M.; Whitburn, S.; Clarisse, L.; Cadypereira, K.; Clerbaux, C.; Coheur, P. F.; Erisman, J. W. NH<sub>3</sub> emissions from large point sources derived from CrIS and IASI satellite observations. *Atmos. Chem. Phys.* **2019**, *19*, 12261–12293.
- (24) McKeever, J.; Durak, B. O. A.; Gains, D.; Varon, D. J.; Germain, S.; Sloan, J. J. GHGSat-D: Greenhouse Gas Plume Imaging and Quantification from Space Using a Fabry-Perot Imaging Spectrometer. Abstract presented at the American Geophysical Union 2017 Fall Meeting, New Orleans, LA, 2017, Dec 11–15, 2017.
- (25) Rodgers, C. D. *Inverse Methods for Atmospheric Sounding: Theory and Practice*; World Scientific, 2000; Vol. 2.
- (26) Gordon, I. E.; Rothman, L. S.; Hill, C.; Kochanov, R. V.; Tan, Y.; Bernath, P. F.; Birk, M.; Boudon, V.; Campargue, A.; Chance, K. V.; Drouin, B. J.; Flaud, J.-M.; Gamache, R. R.; Hodges, J. T.; Jacquemart, D.; Perevalov, V. I.; Perrin, A.; Shine, K. P.; Smith, M.-A. H.; Tennyson, J.; Toon, G. C.; Tran, H.; Tyuterev, V. G.; Barbe, A.; Császár, A. G.; Devi, V. M.; Furtenbacher, T.; Harrison, J. J.; Hartmann, J.-M.; Jolly, A.; Johnson, T. J.; Karman, T.; Kleiner, I.; Kyuberis, A. A.; Loos, J.; Lyulin, O. M.; Massie, S. T.; Mikhailenko, S. N.; Moazzen-Ahmadi, N.; Müller, H. S. P.; Naumenko, O. V.; Nikitin, A. V.; Polyansky, O. L.; Rey, M.; Rotger, M.; Sharpe, S. W.; Sung, K.; Starikova, E.; Tashkun, S. A.; Auwera, J. V.; Wagner, G.; Wilzewski, J.; Wcislo, P.; Yu, S.; Zak, E. J. The HITRAN2016 Molecular Spectroscopic Database. *J. Quant. Spectrosc. Radiat. Transfer* **2017**, *203*, 3–69.
- (27) United States National Aeronautics and Space Agency. *U.S. Standard Atmosphere*, 1976 (Technical Report NASA-TM-X-74335, NASA, 1976). Available at <https://ntrs.nasa.gov/search.jsp?R=19770009539>.
- (28) China State Administration of Coal Mine Safety. *Compilation of National Coal Mine Gas Level Identification for 2011*; National Coal Mine Safety Supervision Bureau, 2019.
- (29) Ong, C.; Day, S.; Halliburton, B.; Marvig, P.; White, S. *Regional Methane Emissions In NSW CSG Basins Final Report*; CSIRO: Australia, 2017.
- (30) Hill, T.; Nassar, R. Pixel size and revisit rate requirements for monitoring power plant CO<sub>2</sub> emissions from space. *Remote Sens.* **2019**, *11*, 1608.
- (31) Jongaramrungruang, S.; Frankenberg, C.; Matheou, G.; Thorpe, A.; Thompson, D. R.; Kuai, L.; Duren, R. Towards accurate methane point-source quantification from high-resolution 2-D plume imagery. *Atmos. Meas. Tech.* **2019**, *12*, 6667–6681.
- (32) Varon, D. J.; Jacob, D. J.; McKeever, J.; Jervis, D.; Durak, B. O. A.; Xia, Y.; Huang, Y. Quantifying methane point sources from fine-scale satellite observations of atmospheric methane plumes. *Atmos. Meas. Tech.* **2018**, *11*, 5673–5686.
- (33) Molod, A.; Takacs, L.; Suarez, M.; Bacmeister, J.; In-Sun, S.; Eichmann, A. *The GEOS-5 Atmospheric General Circulation Model: Mean Climate and Development from MERRA to Fortuna* Technical Report Series on Global Modeling and Data Assimilation; NASA, 2012; Vol. 28.
- (34) DarkSky. DarkSky weather application programming interface (API). <https://darksky.net/dev> (accessed on May 9, 2019).
- (35) Horel, J.; Splitt, M.; Dunn, L.; Pechmann, J.; White, B.; Ciliberti, C.; Lazarus, S.; Slemmer, J.; Zaff, D.; Burks, J. MesoWest: Cooperative Mesonet in the Western United States. *Bull. Am. Meteorol. Soc.* **2002**, *83*, 211–225.
- (36) Nelder, J. A.; Mead, R. A Simplex Method for Function Minimization. *Comput. J.* **1965**, *7*, 308–313.
- (37) Lagarias, J. C.; Reeds, J. A.; Wright, M. H.; Wright, P. E. Convergence Properties of the Nelder-Mead Simplex Method in Low Dimensions. *SIAM J. Optim.* **1998**, *9*, 112–147.
- (38) White, W.; Anderson, J.; Blumenthal, D.; Husar, R.; Gillani, N.; Husar, J.; Wilson, W. Formation and transport of secondary air pollutants: ozone and aerosols in the St. Louis urban plume. *Science* **1976**, *194*, 187–189.
- (39) Krings, T.; Gerilowski, K.; Buchwitz, M.; Reuter, M.; Tretner, A.; Erzinger, J.; Heinze, D.; Pfleiderer, U.; Burrows, J. P.; Bovensmann, H. MAMAP – a new spectrometer system for column-averaged methane and carbon dioxide observations from aircraft: retrieval algorithm and first inversions for point source emission rates. *Atmos. Meas. Tech.* **2011**, *4*, 1735–1758.
- (40) United States Environmental Protection Agency (EPA). Facility Level Information on Greenhouse Gases Tool (FLIGHT), 2017. <https://ghgdata.epa.gov/ghgp/service/html/2017?id=1009342&et=undefined> via <https://ghgdata.epa.gov/ghgp/main.do> (accessed on July 1, 2019).
- (41) Cardno. Environmental Assessment Appin Colliery Area 7 Goaf Gas Drainage Project, 2009. [https://www.south32.net/docs/default-source/illawarra-coal/bulli-seam-operations/appin/appin-surface-gas-management-project--enviro-asse/environmental-assessment-appin-surface-gas-management-project.pdf?sfvrsn=321a9200\\_4](https://www.south32.net/docs/default-source/illawarra-coal/bulli-seam-operations/appin/appin-surface-gas-management-project--enviro-asse/environmental-assessment-appin-surface-gas-management-project.pdf?sfvrsn=321a9200_4) (accessed on Feb 14, 2020).
- (42) Jervis, D.; McKeever, J.; Strupler, M.; Gains, D.; Tarrant, E.; Germain, S. Rapid Design, Build and Characterization Cycle of the GHGSat Constellation. Abstract presented at the American Geophysical Union 2019 Fall Meeting, San Francisco, CA, Dec 9–13, 2019.
- (43) Cusworth, D. H.; Jacob, D. J.; Varon, D. J.; Chan Miller, C.; Liu, X.; Chance, K.; Thorpe, A. K.; Duren, R. M.; Miller, C. E.; Thompson, D. R.; Frankenberg, C.; Guanter, L.; Randles, C. A. Potential of next-generation imaging spectrometers to detect and quantify methane point sources from space. *Atmos. Meas. Tech.* **2019**, *12*, 5655–5668.